Research Article

Ghost resonance in anisotropic materials: negative refractive index and evanescent field enhancement in lossless media

Evgenii Narimanov*

Purdue University, School of Electrical and Computer Engineering, Birck Nanotechnology Center, West Lafayette, Indiana, United States

Abstract. We show that dielectric waveguides formed by materials with strong optical anisotropy support electromagnetic waves that combine the properties of propagating and evanescent fields. These "ghost waves" are created in tangent bifurcations that "annihilate" pairs of positive- and negative-index modes and represent the optical analogue of the "ghost orbits" in the quantum theory of nonintegrable dynamical systems. Ghost waves can be resonantly coupled to the incident evanescent field, which then grows exponentially through the anisotropic media—as in the case of negative index materials. As ghost waves are supported by transparent dielectric media, the proposed approach to electromagnetic field enhancement is free from the "curse" of material loss that is inherent to conventional negative index composites.

1 Introduction

Recent development of negative index metamaterials, where the subwavelength structure of the composite unit cell allows simultaneously negative electric and magnetic responses,[1,2] gave rise to the experimental demonstration of such unusual phenomena as negative refraction and backwards wave propagation,[3] electromagnetic cloaking,[4] and subwavelength focusing.[5] Particularly striking is the behavior of the evanescent waves that may show, instead of the expected decay, exponential growth through the negative index medium,[2] which offers the potential to revolutionize near-field optics.[6] However, this effect is only present when the metamaterial unit cell size is much smaller than the wavelength in the medium.[7] As a result, while there are many different realizations of the negative index media—from photonic crystals[8] to coupled Mie resonators[9] to plasmonic composites[10]—it is only the latter class that supports this exponential enhancement of evanescent field.

However, the material loss inherent to plasmonic media, due to the inevitable free-carrier absorption,[11] severely limits the evanescent field enhancement.[12] Despite multiple attempts to remove this stumbling block with new materials[13] or by

incorporating material gain in the composite design,[14] the (nearly) "lossless metal"[15] that would allow the evanescent field control and amplification promised by metamaterial research for nearly two decades since the seminal work of Pendry[2] remains an elusive goal.[13]

In this work, we present an alternative to the plasmonic approach. We demonstrate that strongly anisotropic dielectric waveguides support "ghost waves," which differ from the "regular" propagating and evanescent fields. These ghost waves represent the optical analogue of the ghost orbits[16] in the semiclassical theory of nonintegrable systems, and in the case of waveguide-free propagation (see Fig. 1) can be treated as a special case of nonuniform plane waves.[17] Similar to the surface plasmons in negative index media, these ghost waves can resonantly couple to the incident evanescent field, resulting in its exponential "amplification" across the anisotropic media. However, all the primary components of the dielectric permittivity tensor for the strongly anisotropic media that support the ghost waves can be positive. As a result, the effect can be observed in a transparent and (nearly) lossless dielectric.

Due to the complexity of the fully three-dimensional (3-D) nanofabrication required for metamaterials with simultaneously negative values of dielectric permittivity and magnetic permeability, much attention has been given to the possible alternatives that

---

*Address all correspondence to Evgenii Narimanov, E-mail: evgenii@purdue.edu
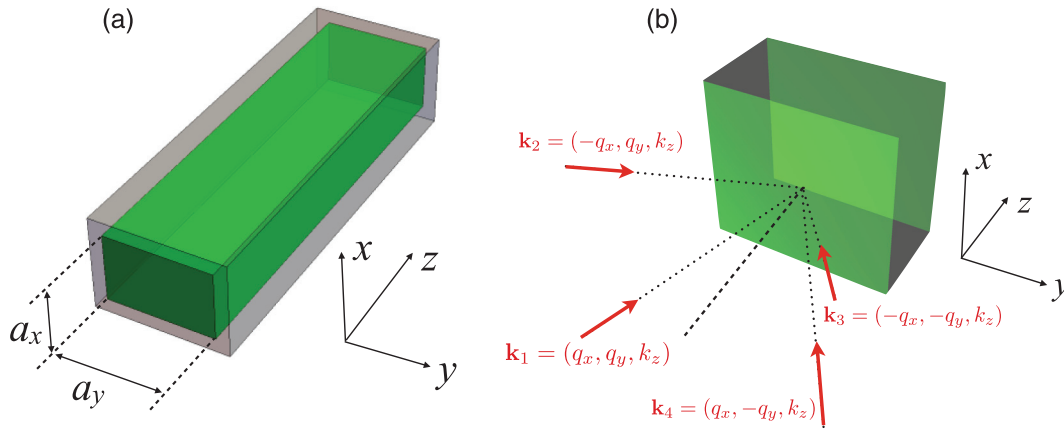
Fig. 1 (a) The schematics of the metal-clad waveguide with the core formed by a biaxial anisotropic dielectric material and (b) the corresponding standing wave pattern formed by the interference of several beams incident onto a slab of the biaxial anisotropic dielectric. Green color in (a) and (b) represents the anisotropic dielectric, whereas the gray region in (a) corresponds to the metallic cladding of the waveguide. For the wavevectors indicated in (b), $q_x = \pi m_x / a_x$, $q_y = \pi m_y / a_y$, with integer values of m_x and m_y the resulting field pattern is identical to that inside the perfect metal-clad waveguide in panel (a).

do not rely on the magnetic response.[18–20] If the desired negative index performance can be limited to propagation in a waveguide, a number of such solutions are possible—using hyperbolic metamaterials,[19] Clarricoats–Waldron geometry,[18] or a waveguide with the core formed by biaxial anisotropic dielectric[20] [see Fig. 1(a)]. Note that in each of these systems, the negative index modes appear in pairs with their positive index counterparts, with each pair born together at the same point of the system phase space at some critical frequency ω_c.

In direct proximity to ω_c, the mode dispersion $\omega(k_z)$ can be treated as a bifurcation diagram with the frequency taking the role of the control parameter. Known as the tangent bifurcation,[21] it is subject to the general rules of nonlinear dynamics,[22] such as the creation of new states in the integer number of pairs. In particular, the actual mode spectra below the tangent bifurcation threshold show the signatures of the so called "ghost orbits" formally defined as extensions of the system dynamics to a higher-dimensional phase space (e.g., extended to complex time and/or spatial coordinates).[16,23–25] We therefore conclude that negative index systems, in a waveguide geometry that does not rely on magnetic response,[18–20] actually support optical equivalents of these "ghosts." Furthermore, such optical ghost waves are essentially different from both positive- and negative-index modes.

Although a waveguide with the core formed by a hyperbolic metamaterial[19] will suffer high-propagation loss due to the absorption in the hyperbolic medium, the approach based on biaxial dielectric media[20] is not so limited. Even with the metallic cladding [see Fig. 1(a)], the propagation loss will be comparatively small,[26,27] due to the relatively small field penetration into the metal. (Note: even at optical frequencies, one finds the effective loss due to the absorption in metallic waveguide cladding on the order of $\text{Im}[K_z]/\text{Re}[K_z] \sim 10^3$, in contrast to $\text{Im}[K_z]/\text{Re}[K_z] \sim 0.1$ in a hyperbolic waveguide.)

Furthermore, the mode pattern in the waveguide that is calculated for the "ideal metal" boundary conditions is identical to the standing wave formed by interfering plane waves incident on a planar dielectric layer that does not at all involve any

high-loss components [see Fig. 1(b)]. [Note that the "ideal metal" boundary condition that sets the tangential electric field to zero, typically used at THz frequencies and below, does not at all actually assume an ideal/lossless metal, but only implies large modulus of the permittivity, regardless of whether it is "lossless" ($|\text{Re}[\epsilon]| \gg \text{Im}[[\epsilon])$ or extremely "lossy" ($|\text{Re}[\epsilon]| \ll \text{Im}[[\epsilon])$; e.g., at GHz frequencies when the use of this approximation is nearly universal,[27] the dielectric permittivity of copper, the material often used for the microwave waveguides, is on the order of $10^8 i$.] With the pattern of multiple beams in Fig. 1(b), the corresponding field profile in the biaxial dielectric becomes identical to that in the (metal-clad) waveguide and the mathematical description that we develop for the ideal metal-clad waveguide is fully applicable to this case. However, as long as the field intensity is sufficiently small to neglect nonlinear effects, the multiple incident beams solution can be expressed as a superposition of the corresponding field profiles for a single incident beam—which implies that the exponential field enhancement due to the ghost resonance predicted in the present work, persists even in the case of a single incident beam.

We will therefore use the waveguide geometry of Fig. 1(a) as the way to clarify the underlying dynamics and the physical origin of the ghost waves, followed by the generalization of our approach to its lossless counterpart of Fig. 1(b).

2 Anisotropic Dielectric Waveguide and Ghost Waves

In the waveguide geometry of Fig. 1(a), the mode calculation is straightforward (see Sec. 6), and we obtain

$$
\begin{aligned}
k_z = \pm \frac{1}{\sqrt{2}} \Bigg\{ & (\epsilon_x + \epsilon_y)\left(\frac{\omega}{c}\right)^2 - \left(1 + \frac{\epsilon_x}{\epsilon_z}\right)q_x^2 - \left(1 + \frac{\epsilon_y}{\epsilon_z}\right)q_y^2 \\
& \pm \Bigg[\left((\epsilon_x - \epsilon_y)\left(\frac{\omega}{c}\right)^2 + \left(1 - \frac{\epsilon_x}{\epsilon_z}\right)q_x^2 - \left(1 - \frac{\epsilon_y}{\epsilon_z}\right)q_y^2\right)^2 \\
& + 4\left(1 - \frac{\epsilon_x}{\epsilon_z}\right)\left(1 - \frac{\epsilon_y}{\epsilon_z}\right)q_x^2 q_y^2 \Bigg]^{\frac{1}{2}} \Bigg\}^{\frac{1}{2}},
\end{aligned}
\tag{1}
$$

where different signs correspond to different "branches" of the dispersion diagram, and ϵ_x, ϵ_y, and ϵ_z are the primary components of the dielectric permittivity tensor in the waveguide core. For the waveguide, $q_x = m_x\pi/a_x$ and $q_y = m_y\pi/a_y$, where a_x and a_y represent the dimensions of the waveguide cross section [see Fig. 1(a)], whereas in the 3-D case of Fig. 1(b) q_x and q_y correspond to the magnitudes of the in-plane momentum components of the incident wave(s). If one of the integers m_x and m_y is equal to zero, the propagating fields are either TE- or TM-polarized, otherwise, the mode has the "hybrid" structure[27] when all six components of the electromagnetic field are nonzero.

Choosing $\hat{y}$ as the direction of the largest permittivity in the (x, y) plane (i.e., $\epsilon_x < \epsilon_y$), from Eq. (1), we find (see Fig. 2) that the system supports negative index modes (with the group velocity $v_z = \partial\omega/\partial k_z < 0$) if and only if

$$\epsilon_x < \epsilon_z < \epsilon_y, \tag{2}$$

and

$$\arctan\left(\frac{\epsilon_x}{\epsilon_y}\sqrt{\frac{\epsilon_y - \epsilon_z}{\epsilon_z - \epsilon_x}}\right) < \varphi < \arctan\left(\sqrt{\frac{\epsilon_y - \epsilon_z}{\epsilon_z - \epsilon_x}}\right), \tag{3}$$

where the angle

$$\varphi \equiv \arctan(q_y/q_x) \tag{4}$$

in the waveguide geometry [Fig. 1(a)] is defined by the dimensions of the waveguide cross section [$\varphi = \arctan(m_y a_x/m_x a_y)$], whereas for the 3-D case [see Fig. 1(b)], the angle φ corresponds to the propagation direction in the (x, y) plane. This is consistent with the results of Ref. 20, where the presence of negative index modes in biaxial anisotropic media waveguides was first pointed out.

Furthermore, when φ is equal to

$$\varphi_D \equiv \arctan\left(\sqrt{\frac{\epsilon_x}{\epsilon_y} \cdot \frac{\epsilon_y - \epsilon_z}{\epsilon_z - \epsilon_x}}\right), \tag{5}$$

we find (see Sec. 7) that the system shows Dirac dispersion point at the frequency

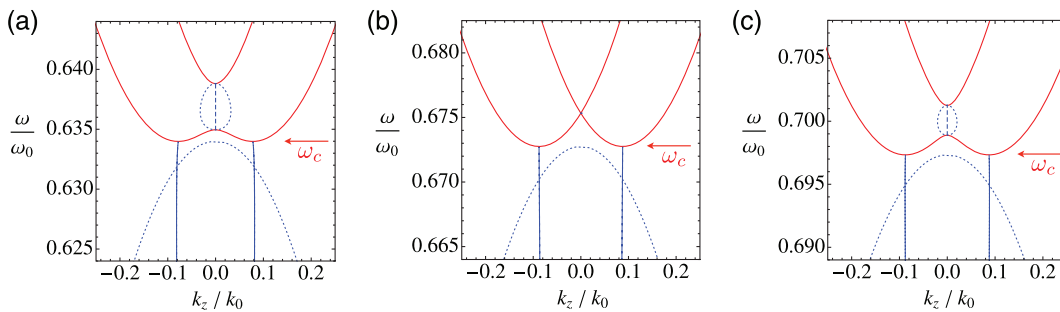$$\omega_D = c\sqrt{\frac{(\epsilon_y - \epsilon_x)}{\epsilon_y(\epsilon_z - \epsilon_x)}} \cdot q_x, \tag{6}$$

as seen in Fig. 2(b). Note that, as follows from Eqs. (5) and (6), the anisotropic waveguide system only shows the Dirac point when all three primary components of its dielectric permittivity tensor are different from each other. The presence of the Dirac point in a strongly anisotropic dielectric system is not at all surprising, as this is the original context for the discovery of the "diabolic points" and the resulting conical diffraction.[29–36]

For a given set of the integers m_x and m_y, or equivalently for a given magnitude of the in-plane momentum on the incident field (q_x, q_y) [see Fig. 1(a)], the biaxial anisotropic dielectric core supports propagating waves only above the critical frequency (see Fig. 2):

$$\omega_c = \frac{c}{\sqrt{\epsilon_y - \epsilon_x}}\left(q_x\sqrt{1 - \frac{\epsilon_x}{\epsilon_z}} + q_y\sqrt{\frac{\epsilon_y}{\epsilon_z} - 1}\right), \tag{7}$$

when two simultaneous tangent bifurcations appear, one at $k_z = k_c$ and the other at $k_z = -k_c$. Here (see Sec. 7),

$$k_c = \frac{1}{\sqrt{\epsilon_z(\epsilon_y - \epsilon_x)}}\left[\epsilon_x(\epsilon_z - \epsilon_y)q_x^2 + \epsilon_y(\epsilon_x - \epsilon_z)q_y^2 \right.$$
$$\left. + (\epsilon_x + \epsilon_y)\sqrt{(\epsilon_z - \epsilon_x)(\epsilon_y - \epsilon_z)}q_x q_y\right]^{1/2} \tag{8}$$

Fig. 2 The dispersion diagrams for the waves supported by sodium nitrite $NaNO_2$, a biaxial anisotropic dielectric with the primary components of the dielectric permittivity tensor[20,28] $\epsilon_x \simeq 1.806$, $\epsilon_y \simeq 2.726$, and $\epsilon_z \simeq 1.991$. The frequency is shown in units of ω_0 and the wavenumber k_z in units of $k \equiv \omega/c$, for (a) $q_x = 0.5k_0$, $q_y = 0.75k_0$; (b) $q_x = 0.5k_0$, $q_y \simeq 0.81k_0$; and (c) $q_x = 0.5k_0$, $q_y = 0.85k_0$, where $k_0 \equiv \omega_0/c$ is the free space wavenumber at the frequency ω_0. The corresponding values of the critical frequency ω_c are marked in each panel. For the waveguide system in Fig. 1(a), $q_x = \pi m_x/a_x$ and $q_y = \pi m/a_y$, where m_x and m_y are the positive integer numbers, whereas for the anisotropic dielectric slab geometry in Fig. 1(b), q_x and q_y correspond to the magnitudes of the (in-plane) x and y components of the incident field wavevector. Note the Dirac point in (b) at the frequency $\omega \approx 0.675\omega_0$. Red lines represent the propagating modes, whereas blue curves correspond to the ghost waves, with dashed and dotted lines showing the real and the imaginary parts of the wavenumber k_z.

creates two pairs of positive- and negative-index modes. However, if—following the standard approach originally developed for the semiclassical dynamics of nonintegrable systems,[16,23–25]—one extends the system phase space to the complex domain, Eq. (1) also yields two pairs of solutions below the critical frequency ω_c, with complex-conjugate wavenumbers that have simultaneously nonzero real and imaginary parts: $\pm k_z' \pm i k_z''$, as shown in Fig. 2 by blue lines. These modes are the optical equivalents of the "ghost" solutions in nonlinear dynamics[16] and will therefore be referred to as the "ghost waves."

Formally, we define the ghost mode as the guided wave with simultaneously nonzero values of the real and imaginary parts of its wavenumber that originates from a tangent bifurcation of two distinct (i.e., not related by symmetry) propagating waves.

As guided waves supported by the dielectric waveguide core can be interpreted in terms of the standing wave solutions of the infinite dielectric medium (see Fig. 1), the concept of the ghost wave can be generalized to the case of (waveguide-free) propagation in three dimensions [see Fig. 1(b)]. For these "generalized" ghost waves, the essentially nonzero value of the plane momentum $\mathbf{q} \equiv (q_x, q_y)$ required by Eqs. (7) and (8) leads to the intensity of a single-ghost wave that is nonuniform across each phase front. In this case, the corresponding ghost modes can, therefore, be considered as a special case of nonuniform waves,[17] where the amplitudes are not constant across the wavefronts.

Note, however, that not every nonuniform wave is a (generalized) ghost wave. Consider, for example, the field of a surface plasmon propagating along a lossy metal–dielectric interface.[10] In the metallic half-space, the corresponding electric field is a nonuniform plane wave, with the intensity that exponentially decays away from the interface along the wavefront that is perpendicular to the interface.[10] While both the real and imaginary parts of the surface plasmon wavenumber are both nonzero in the direction of the propagation, it does not originate from a tangent bifurcation and is not a ghost wave. Note that, as opposed to ghost waves, for the surface plasmon, the Poynting vector in the propagation direction is always nonzero, for any amount of loss.

Ghost waves are also distinct from propagation within the bandgap of a photonic crystal, which show a combination of the oscillations and the exponential decay.[37] In the case of a simple photonic crystal with a one-dimensional (1-D) periodicity, the oscillatory behavior of the electromagnetic field in the bandgap is set by the periodic structure of the composite, and—in contrast to ghost waves—cannot be changed continuously. In a 1-D photonic crystal, these oscillations originate from the behavior of the zero momentum Bloch function at the bandgap edge so that the corresponding (quasi-) momentum in the bandgap is purely imaginary—and thus corresponds to a conventional evanescent wave of an unstructured dielectric.

The situation, however, becomes different in photonic crystals that are patterned in 2-D or 3-D. There, if the band edge corresponds to the center of the Brillouin zone (Γ-point), the resulting modes in the bandgap can still be treated as generalizations of the "regular" evanescent modes and remain unrelated to ghost waves. However, when the propagating band edge is not at the center of the Brillouin zone (but corresponds to the X or the L points in the case of a face-centered cubic lattice of close-packed dielectric spheres[37]), modes in the bandgap will show the behavior similar to that of the ghost waves.
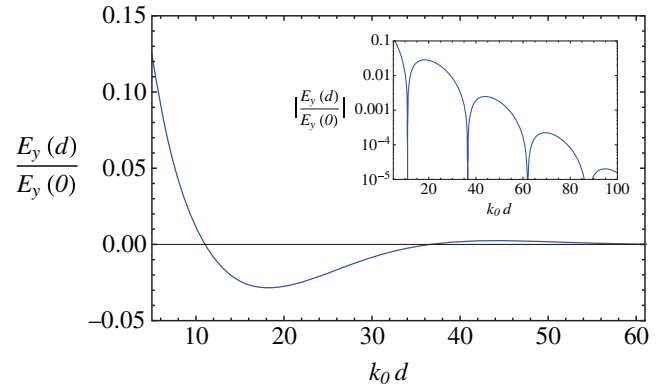
Fig. 3 The y component of the electric field in the biaxial anisotropic dielectric, in either the waveguide or the slab geometry [see the schematics in Figs. 4(a) and 4(b)], as a function of the length d. The dielectric occupies the range $0 < z < d$, $q_x \simeq 0.79 k_0$, and $q_y \simeq 0.185 k_0$. The surrounding medium is air, and the anisotropic dielectric is sodium nitrite NaNO$_2$. The inset shows the field in the logarithmic scale. Note the combination of the exponential decay and the oscillatory behavior, characteristic of the ghost waves.

3 Ghost Resonance

Qualitatively, the ghost fields combine the properties of the evanescent and propagating waves. Similar to the evanescent modes, the intensity of the ghost waves exponentially decays with distance. On the other hand, the ghost waves also oscillate, which allows one to use conventional interference to control their propagation. The latter behavior is illustrated in Fig. 3, corresponding to a biaxial dielectric of length d inserted into the originally air-filled metal waveguide [see Fig. 4(a)] that is operating below the cut-off frequency ω_c, or to a biaxial dielectric slab of the thickness d [see Fig. 4(b)]. As a function of the length d, the field in the dielectric shows both the exponential decay and the oscillations, consistent with the picture of the excitation of the ghost waves.

Similar to the conventional evanescent modes in a waveguide geometry, a single-ghost wave does not carry energy, with the zero projection of the Poynting vector S_z along the axis of the waveguide:

$$\mathbf{S}_z^{\text{ghost}} = 0. \tag{9}$$

However, the essential difference of the ghost waves from both the propagating and the evanescent fields, clearly manifests itself in the wave impedance Z, defined as the ratio of the tangential components of the electric and magnetic fields:[27]

$$Z_x = \frac{E_x}{H_y}, \tag{10}$$

$$Z_y = -\frac{E_y}{H_x}. \tag{11}$$

Although the wave impedance is real for the propagating modes and purely imaginary for the evanescent fields, for the ghost waves both its real and imaginary parts are nonzero:
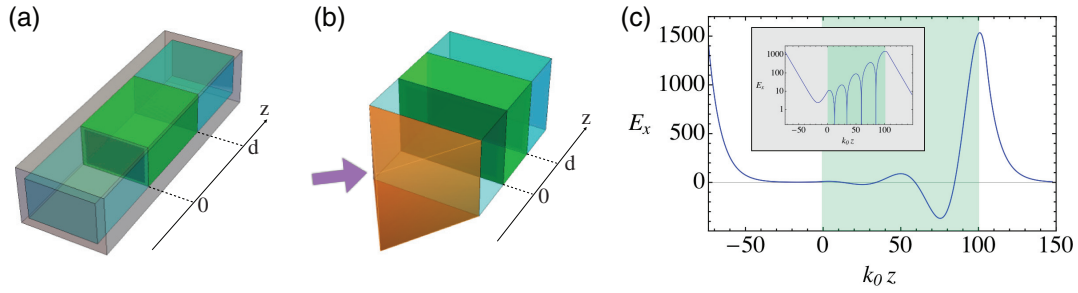
Fig. 4 Evanescent field enhancement at the ghost resonance in the (a) waveguide and (b) slab geometry. Green region represents the biaxial anisotropic dielectric, blue is the surrounding dielectric medium, and orange is the high-index prism coupler. (c) The x component of the electric field, with the linear scale in the main plot and the logarithmic scale in the inset. The green-shaded areas in (c) and its inset indicate the range occupied by the anisotropic dielectric medium. In this example, the anisotropic dielectric is sodium nitrite $NaNO_2$ with the width $d \simeq 16.18\lambda_0$, and the surrounding medium is dielectric with the permittivity of $\epsilon_0 = 2.01$ while $q_x \simeq 0.793k_0$ and $q_y \simeq 1.182k_0$. Note the dramatic enhancement of the incident evanescent field in the anisotropic material.

$$Z_x = \frac{\omega}{ck_z} \cdot \frac{\epsilon_z - \left(\frac{cq}{\omega}\right)^2}{\epsilon_z + (\epsilon_x - \epsilon_y) \cdot \frac{\left(\frac{cq}{\omega}\right)^2}{\epsilon_y - \left(\frac{cq}{\omega}\right)^2 - \left(\frac{ck_z}{\omega}\right)^2}}, \quad (12)$$

$$Z_y = \frac{\omega}{ck_z} \cdot \frac{\epsilon_z - \left(\frac{cq}{\omega}\right)^2}{\epsilon_z - (\epsilon_x - \epsilon_y) \cdot \frac{\left(\frac{cq}{\omega}\right)^2}{\epsilon_x - \left(\frac{cq}{\omega}\right)^2 - \left(\frac{ck_z}{\omega}\right)^2}}, \quad (13)$$

where

$$q \equiv \sqrt{q_x^2 + q_y^2}. \quad (14)$$

(Note that, for the ghost waves $k_z = k_z' + ik_z''$, $k_z' \neq 0$ and $k_z'' \neq 0$ at the same time.)

The most important feature of the ghost waves, however, is that they can be resonantly coupled to the incident evanescent field. In this regime, within the biaxial dielectric supporting the ghost waves, the evanescent decay is replaced by the exponential increase of the field amplitude—as seen in Fig. 4. Aside from the oscillatory behavior of the ghost waves "under" the exponential envelope, this behavior is similar to that in the negative index superlens that also shows exponential "amplification" of the evanescent field.[2] However, as the ghost waves can be supported by a dielectric slab that does not include any lossy components such as metals [see Fig. 4(b)], the ghost waves are free from the constraint of the material absorption that severely limits the superlens performance.

Although at the resonance condition ghost waves lead to the exponential growth of the field in both the waveguide [Fig. 4(a)] and slab [Fig. 4(b)] geometries, the corresponding behavior away from the resonance is substantially different. In the waveguide geometry, as a function of frequency, the transmission coefficient for the incident evanescent field shows a very sharp resonance, which becomes progressively narrower with the increase of the width of the anisotropic layer d (see Fig. 5). This is consistent with the general behavior found in resonant systems—when an increase of the field enhancement comes at the expense of reduced frequency bandwidth.

In contrast to this behavior, in the slab geometry of Fig. 4(b), the resonance condition is defined in terms of the angle of incidence θ—see Fig. 6(a). The ghost resonance in the slab geometry is illustrated in Fig. 6, where we plot the modulus of the normal into interface field component $|E_z|$ in the geometry of Fig. 4(b) at the angle of incidence corresponding to the resonant coupling. In this regime, as long as the frequency dispersion of the dielectric permittivities of anisotropic slab and surrounding dielectric can be neglected (which is often the case in transparent media), the ghost resonance [see Fig. 6(b)] persists in a broad frequency range.

This behavior is dramatically different from the usual trade-off between the field enhancement and frequency bandwidth that is nearly universal in resonant systems and offers many
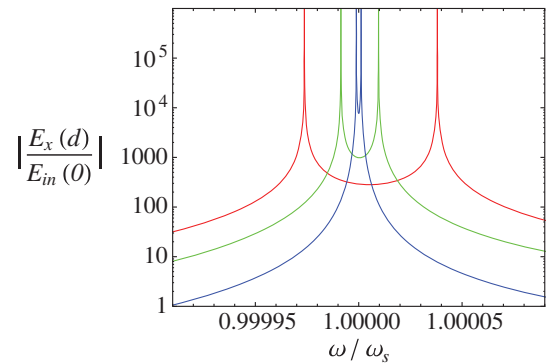
Fig. 5 The frequency spectrum of the "transmitted" field $E_x(d)$, normalized to the amplitude of the incident field E_{in} at $z = 0$ [see the schematics in Figs. 4(a) and 4(b)], for the sodium nitrite biaxial crystal [green region in Fig. 4(a)], surrounded by an isotropic dielectric with the permittivity $\epsilon = 2.01$ [shown in blue in Figs. 4(a) and 4(b)], with $q_x \simeq 0.79k_0$ and $q_y \simeq 1.18k_0$. The length of the biaxial dielectric $d \simeq 7.96\lambda_0$ (red curve), $d \simeq 11.94\lambda_0$ (green curve), and $d \simeq 16.78\lambda_0$ (blue curve). The frequency is normalized to the value corresponding to the surface state at a single-sodium nitrite–isotropic dielectric interface, given by Eq. (15).

(a) (b)
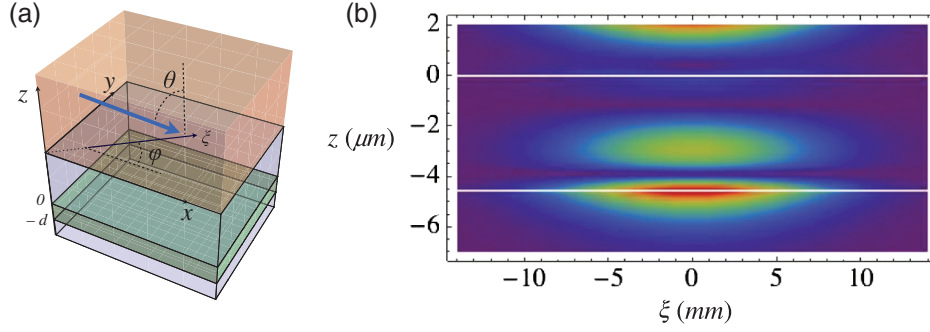
Fig. 6 (a) The schematic of the coordinate system used in the slab geometry of Fig. 4(b). Orange volume corresponds to the high-index prism coupler, and green layer is the biaxial dielectric. Light blue regions represent the isotropic dielectric surrounding the biaxial medium. Blue arrow shows the direction of the incident Gaussian beam, with the angle θ above the critical angle of the total internal reflection θ_c of the coupler—isotropic dielectric interface. (b) The modulus of the normal to the interface electric field component $|E_z|$ (in false-color representation) at the resonance condition. The incident beam direction is defined by the angles $\phi = 56.15$ deg and $\theta \approx 46.462$ deg, the biaxial medium is sodium nitrite NaNO$_2$, the high-index prism is made of gadolinium gallium garnet ($\epsilon_{GGG} \approx 1.963$), and the permittivity of the isotropic dielectric $\epsilon_0 = 2.01$. The wavelength is $\lambda_0 = 650$ nm, and the biaxial layer thickness $d \approx 7\lambda_0 \approx 4.57$ μm.

intriguing possibilities for applications in nonlinear optics—such as supercontinuum generation.

However, the ghost resonance in the slab geometry (see Fig. 6) imposes very stringent requirements on the angle of incidence θ. With a small deviation of the incidence angle θ from the resonance condition, the field enhancement is rapidly suppressed (as illustrated in Fig. 7).

Although ghost resonance is very sensitive to the deviations in the angle of incidence, it is robust to changes in polarization. The reason for this behavior is that, in the corresponding eigenstates in the slab geometry (due to the absence of uniaxial symmetry in the dielectric) all (six) of the field components are essentially nonzero. As a result, ghost states can couple to both s- and p-polarized incident light.

4 Physical Origin of the Ghost Resonance

With the deep connection of light propagation in anisotropic dielectric waveguides to field enhancement and super-resolution imaging with negative index media, it should not come as a surprise that the fundamental physical origin of the exponential "amplification" in biaxial media is also similar to that in the negative index superlens—it is the resonant coupling to surface states supported by the medium.[38] In the case of the negative index material–air interface, the surface state in question is the surface plasmon polariton,[10,38] whereas in the biaxial dielectric it is the surface mode at the isotropic dielectric–anisotropic dielectric interface, shown in Fig. 8. This surface mode is formed by the "regular" evanescent field in the isotropic side and by the decaying ghost wave in the biaxial medium (note the oscillatory behavior for $z > 0$ in Fig. 8). In the limit $\epsilon_z \to \epsilon_x$, this mode reduces to the well-known Dyakonov surface wave that was originally introduced for the interface of an isotropic medium with a uniaxial dielectric.[39–41]

At the interface of the biaxial medium and the isotropic dielectric with the permittivity ϵ_0, the surface state dispersion $\omega_s(q_x, q_y)$ is defined by the following equation (see Sec. 8):

$$
\kappa_0(\kappa_+ + \kappa_-)\left\{\kappa_+\kappa_- + \frac{\epsilon_x\epsilon_y}{\epsilon_0}\left[\frac{q_x^2}{\epsilon_y} + \frac{q_y^2}{\epsilon_x} - \left(\frac{\omega_s}{c}\right)^2\right]\right\}
$$
$$
+ \kappa_+\kappa_-\left[\left(1 + \frac{\epsilon_x}{\epsilon_0}\right)q_x^2 + \left(1 + \frac{\epsilon_y}{\epsilon_0}\right)q_y^2 - (\epsilon_x + \epsilon_y)\left(\frac{\omega_s}{c}\right)^2\right]
$$
$$
+ \left\{\kappa_+^2\kappa_-^2 + \frac{\epsilon_x\epsilon_y}{\epsilon_0}\kappa_0^2\left[\frac{q_x^2}{\epsilon_y} + \frac{q_y^2}{\epsilon_x} - \left(\frac{\omega_s}{c}\right)^2\right]\right\} = 0, \quad (15)
$$

where
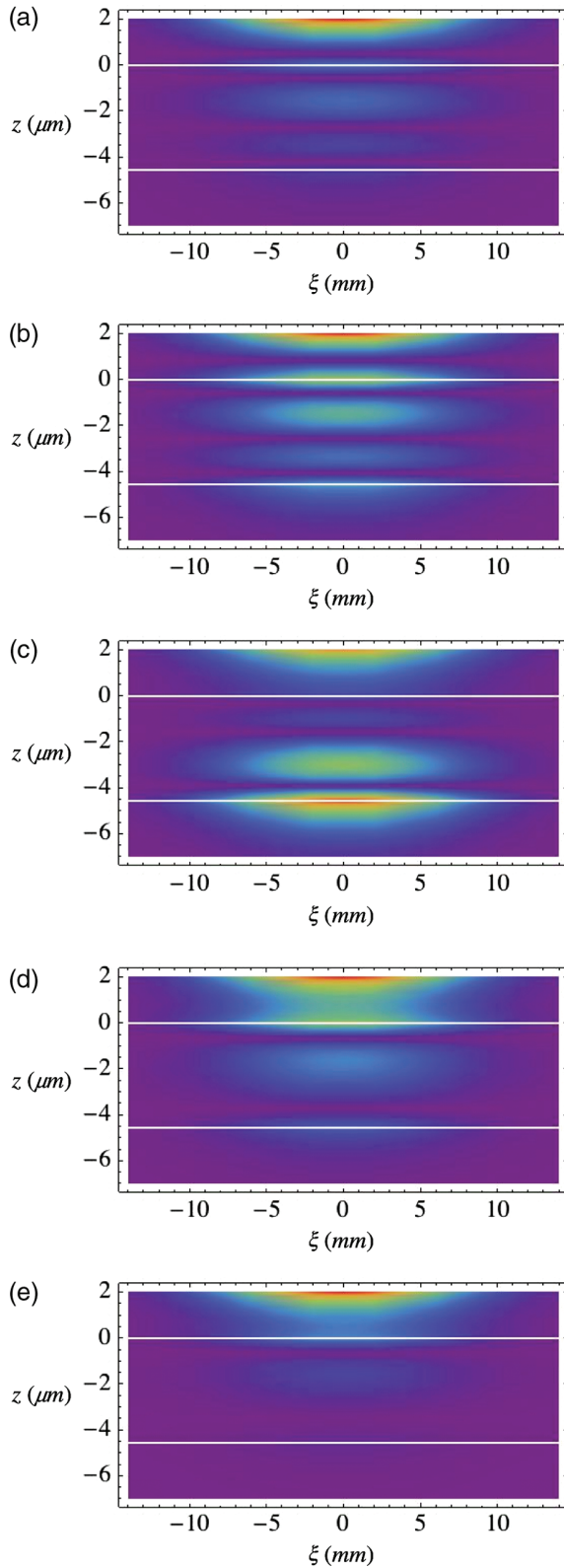
$$
\kappa_0 = \sqrt{q_x^2 + q_y^2 - \epsilon_0\left(\frac{\omega_s}{c}\right)^2}, \quad (16)
$$

and

$$
\kappa_{\pm} = \frac{1}{\sqrt{2}}\left\{\left(1 + \frac{\epsilon_x}{\epsilon_z}\right)q_x^2 + \left(1 + \frac{\epsilon_y}{\epsilon_z}\right)q_y^2 - (\epsilon_x + \epsilon_y)\left(\frac{\omega_s}{c}\right)^2\right.
$$
$$
\pm \left[\left((\epsilon_x - \epsilon_y)\left(\frac{\omega_s}{c}\right)^2 + \left(1 - \frac{\epsilon_x}{\epsilon_z}\right)q_x^2 - \left(1 - \frac{\epsilon_y}{\epsilon_z}\right)q_y^2\right)^2\right.
$$
$$
\left.\left. + 4\left(1 - \frac{\epsilon_x}{\epsilon_z}\right)\left(1 - \frac{\epsilon_y}{\epsilon_z}\right)q_x^2q_y^2\right]^{\frac{1}{2}}\right\}^{\frac{1}{2}}. \quad (17)
$$

Note that Eq. (15) has a solution with $\text{Re}(k_0) > 0$ and $\text{Re}(k_\pm) > 0$ (corresponding to the surface wave) only when $\epsilon_z < \epsilon_0 < \epsilon_y$.

The signatures of the surface waves are clearly visible in Fig. 5, which shows the transmission coefficient for the incident evanescent field as a function of frequency, for different values of the width of the anisotropic layer d. Note that close to the center of the ghost resonance its profile shows the double-peak structure, corresponding to the symmetric and antisymmetric combination of the surface states at the two interfaces. An increase of the width of the anisotropic layer leads to the reduction of the coupling between these two surface states, which suppresses the splitting between the peaks (see Fig. 5).
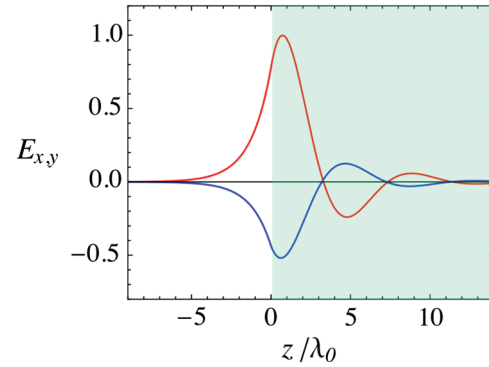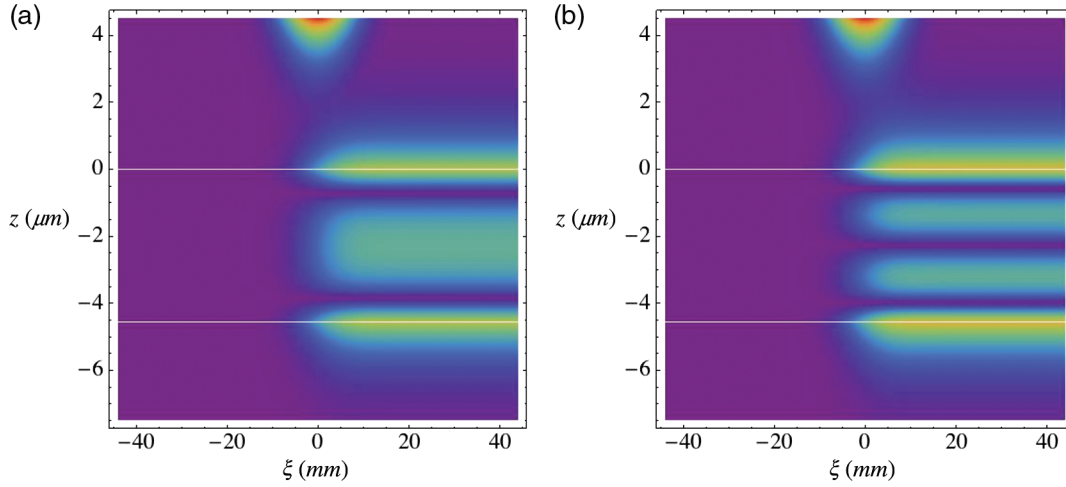
Fig. 8 The surface state profile at the interface of isotropic dielectric ($z < 0$) with biaxial anisotropic medium ($z > 0$). The red and blue lines, respectively, correspond to the x and y components of the electric field. The biaxial dielectric is sodium nitrite NaNO$_2$ ($\epsilon_x \simeq 1.806$, $\epsilon_y \simeq 2.726$, and $\epsilon_z \simeq 1.991$), and the permittivity of the isotropic medium $\epsilon = 2.01$, whereas $q_x \simeq 0.793 k_0$ and $q_y \simeq 1.182 k_0$. Note the simple exponential decay in the isotropic material and oscillatory behavior in the biaxial medium.

To further illustrate this behavior in Fig. 9, we plot the electric field E_z for the parameters corresponding to the excitation of the symmetric [see Fig. 9(a)] and antisymmetric [Fig. 9(b)] combinations of the Dyakonov surface states at the biaxial–isotropic dielectric interfaces.

Although for the idealized model of the system (lossless dielectric, perfect planar interfaces, and no bulk defects leading to light scattering), the transmission coefficient at the ghost resonance can be arbitrarily high, any disorder will limit the field enhancement. Although material imperfections and their impact can be, at least in theory, reduced to an arbitrarily small level, there is also a fundamental limit to the performance of the proposed "ghost resonator," imposed by the inherent nonlocality of the electromagnetic response due to the finite size of the material unit cell. For natural dielectric media, the corresponding correction to the permittivity scales[42] as $(k_0 a_0)^2$, where a_0 is on the order of the atomic/molecular size, leading to the fundamental limit on the evanescent field enhancement $\sim 1/(k_0 a_0)^2 \sim 10^6$.

5 Conclusions

The strong local field enhancement at or near the condition of resonant coupling to the ghost waves can find many applications from optical sensing, e.g., in Kretschmann geometry, where a small variation of the refraction index of the isotropic medium surrounding the biaxial slab would lead to a dramatic change of the observed reflectivity, to nonlinear-optical phenomena. The biaxial crystal anisotropy needed to support the ghost waves naturally fits the requirements of nonlinear optics, as such strongly anisotropic crystalline materials (e.g., sodium nitrite used in Figs. 2–9) generally possess high second-order nonlinear susceptibilities. The combination of relatively large values of χ_2 in strongly anisotropic dielectrics with the exponential field enhancement by several orders of magnitude in a simple planar geometry makes the ghost wave resonance a useful tool for nonlinear optics—from second harmonic generation to higher-order nonlinear effects such as supercontinuum generation.

Fig. 7 The evolution of the electromagnetic field in the slab geometry of Fig. 4(b), near the "ghost resonance," with the incidence angle θ: (a) 46.42 deg, (b) 46.44 deg, (c) 46.46 deg, (d) 46.48 deg, and (e) 46.5 deg. The angle ϕ, the system spatial dimensions, and the material parameters are the same as in Fig. 6. Note that the entire sequence (a) to (e) corresponds to the variation of the incidence angle θ by <0.1 deg.

Fig. 9 The modulus of the electric field component $|E_z|$ (in false-color representation), for the resonant excitation of the (a) symmetric and (b) antisymmetric superpositions of the Dyakonov surface waves at the two biaxial–isotropic dielectric interfaces in the slab geometry of Figs. 4(b) and 6(a). The incidence angle θ is equal to (a) 46.4681 deg and (b) 46.4524 deg. The angle ϕ, the system spatial dimensions, and the material parameters are the same as in Figs. 6 and 7.

Note that the waveguide geometry that we used to introduce the concepts of ghost waves and ghost resonances naturally fits the requirements of nonlinear optics and optoelectronics, where waveguide confinement is essential to further concentrate optical intensity in the former case and allows for dense component integration in the latter.

A dielectric system that supports ghost waves may also find imaging applications; similar to the superlens,[2] it can enhance the evanescent fields scattered by an object that carry the information about its subwavelength structure. However, as opposed to the surface plasmons at the boundary of a negative medium with $\epsilon = -1$, $\mu = -1$, when these modes can support arbitrary high in-plane wavenumbers, the surface waves at the biaxial–isotropic interface do not show a similar degeneracy. As a result, the biaxial dielectric system will only perform as a lossless superlens that operates away from the $n = -1$ condition, with the corresponding loss of the resolution.[43]

In conclusion, we have demonstrated that biaxial anisotropic media support ghost waves that combine the properties of the propagating and the evanescent fields. We have shown that resonant coupling of the ghost modes can be used to exponentially enhance and modulate the incident evanescent waves, thus opening a new way for near-field control and manipulation.

6 Appendix A

For a wave propagating along axis z of waveguide in Fig. 1, its electromagnetic field can be represented as

$$\mathbf{E}(\mathbf{r}, t) = \mathbf{E_q}(x, y) \cdot \exp(ik_z z - i\omega t), \tag{18}$$

$$\mathbf{B}(\mathbf{r}, t) = \mathbf{B_q}(x, y) \cdot \exp(ik_z z - i\omega t), \tag{19}$$

where

$$\mathbf{E_q}(x, y) = [e_x \cdot \cos(q_x x) \sin(q_y y), \; e_y \cdot \sin(q_x x) \cos(q_y y), \\ e_z \cdot \sin(q_x x) \sin(q_y y)], \tag{20}$$

and

$$\mathbf{B_q}(x, y) = [b_x \cdot \sin(q_x x) \cos(q_y y), \; b_y \cdot \cos(q_x x) \sin(q_y y), \\ b_z \cdot \cos(q_x x) \cos(q_y y)]. \tag{21}$$

Substituting Eqs. (18)–(21) into Maxwell's equations, we obtain

$$b_x = -\frac{c}{\omega}(k_z e_y + i q_y e_z), \tag{22}$$

$$b_y = \frac{c}{\omega}(k_z e_x + i q_x e_z), \tag{23}$$

$$b_z = \frac{c}{\omega}(i q_y e_x - i q_x e_y), \tag{24}$$

and

$$\mathcal{M} \begin{pmatrix} e_x \\ e_y \\ e_z \end{pmatrix} = 0, \tag{25}$$

where

$$\mathcal{M} \equiv \begin{bmatrix} \Delta_x(k_z) & q_x q_y & -ik_z q_x \\ q_x q_y & \Delta_y(k_z) & -ik_z q_y \\ ik_z q_x & ik_z q_y & \Delta_z(k_z) \end{bmatrix}, \tag{26}$$

and

$$\Delta_x(\kappa) = \epsilon_x \left(\frac{\omega}{c}\right)^2 - q_y^2 - k_z^2, \tag{27}$$

$$\Delta_y(\kappa) = \epsilon_y \left(\frac{\omega}{c}\right)^2 - q_x^2 - k_z^2, \tag{28}$$

$$\Delta_z(\kappa) = \epsilon_z \left(\frac{\omega}{c}\right)^2 - q_x^2 - q_y^2. \tag{29}$$

From Eq. (25), we obtain

$$\det(\mathcal{M}) = 0, \tag{30}$$

which yields

$$\epsilon_z \cdot k_z^4 - \left[(\epsilon_x + \epsilon_y) \cdot \left(\frac{\omega}{c}\right)^2 - (\epsilon_x + \epsilon_z) \cdot q_x^2 - (\epsilon_y + \epsilon_z) \cdot q_y^2\right]$$
$$\cdot k_z^2 + \left[\epsilon_z \left(\frac{\omega}{c}\right)^2 - q_x^2 - q_y^2\right]\left[\epsilon_x \epsilon_y \left(\frac{\omega}{c}\right)^2 - \epsilon_x q_x^2 - \epsilon_y q_y^2\right] = 0. \tag{31}$$

Equation (31) is a quadratic equation for κ^2, with the straightforward solution

$$k_\pm^2 = \frac{1}{2}\left[(\epsilon_x + \epsilon_y) \cdot \left(\frac{\omega}{c}\right)^2 - \frac{\epsilon_x + \epsilon_z}{\epsilon_z} q_x^2 - \frac{\epsilon_y + \epsilon_z}{\epsilon_z} q_y^2 \pm \sqrt{D}\right], \tag{32}$$

where the discriminant

$$D = \left[(\epsilon_x - \epsilon_y)\left(\frac{\omega}{c}\right)^2 + \frac{\epsilon_z - \epsilon_x}{\epsilon_z} q_x^2 + \frac{\epsilon_y - \epsilon_z}{\epsilon_z} q_y^2\right]^2$$
$$+ 4 \cdot \frac{(\epsilon_x - \epsilon_z) \cdot (\epsilon_y - \epsilon_z)}{\epsilon_z^2} q_x^2 q_y^2. \tag{33}$$

7 Appendix B

With the dispersion defined by Eq. (1) or equivalently Eqs. (32) and (33), the propagating modes are only present above the critical frequency ω_c defined by

$$D(\omega_c) = 0, \tag{34}$$

which, for $\epsilon_x < \epsilon_z < \epsilon_y$, yields

$$\omega_c = \frac{c}{\sqrt{\epsilon_y - \epsilon_x}}\left(\sqrt{1 - \frac{\epsilon_x}{\epsilon_z}} \cdot q_x + \sqrt{\frac{\epsilon_y}{\epsilon_z} - 1} \cdot q_y\right), \tag{35}$$

with the corresponding critical wavenumber

$$k_c = \frac{1}{\sqrt{\epsilon_z(\epsilon_y - \epsilon_x)}}\left[\epsilon_x(\epsilon_z - \epsilon_y)q_x^2 + \epsilon_y(\epsilon_x - \epsilon_z)q_y^2\right.$$
$$\left. + \sqrt{(\epsilon_z - \epsilon_x)(\epsilon_y - \epsilon_z)}(\epsilon_x + \epsilon_y)q_x q_y\right]^{1/2}. \tag{36}$$

The two tangent bifurcations in the dispersion diagram of Figs. 2(a) and 2(c) that occur at the zero of the momentum k_z at the frequencies $\omega_2^\pm$, correspond to

$$k_-(\omega_2^\pm) = 0. \tag{37}$$

Substituting Eq. (32) into Eq. (37), we obtain

$$\omega_2^+ = c\sqrt{\frac{q_x^2 + q_y^2}{\epsilon_z}}, \tag{38}$$

$$\omega_2^- = c\sqrt{\frac{q_x^2}{\epsilon_y} + \frac{q_y^2}{\epsilon_x}}. \tag{39}$$

The necessary and sufficient condition for the presence of the negative index modes in the waveguide is

$$\omega_c < \min(\omega_2^+, \omega_2^-), \tag{40}$$

which leads to Eqs. (2) and (3).

When the frequency gap between ω_2^+ and ω_2^- collapses to zero, the dispersion diagram shows the Dirac point [see Fig. 2(b)]. For the corresponding values of q_x and q_y, we find

$$q_y = \sqrt{\frac{\epsilon_x}{\epsilon_y} \cdot \frac{\epsilon_y - \epsilon_z}{\epsilon_z - \epsilon_x}} \cdot q_x, \tag{41}$$

so that the propagation angle φ in the plane of the isotropic–biaxial interface [see Fig. 6(a)] is given by

$$\varphi_D \equiv \arctan \left.\frac{q_y}{q_x}\right|_{\omega_D} = \arctan \sqrt{\frac{\epsilon_x}{\epsilon_y} \cdot \frac{\epsilon_y - \epsilon_z}{\epsilon_z - \epsilon_x}}, \tag{42}$$

and the frequency

$$\omega_D = c\sqrt{\frac{(\epsilon_y - \epsilon_x)}{\epsilon_y(\epsilon_z - \epsilon_x)}} \cdot q_x \tag{43}$$

$$= c\sqrt{\frac{(\epsilon_y - \epsilon_x)}{\epsilon_x(\epsilon_y - \epsilon_z)}} \cdot q_y. \tag{44}$$

8 Appendix C

Assuming that the interface at $z = 0$ separates transparent isotropic medium with the permittivity ϵ_0 at $z < 0$ from biaxial anisotropic dielectric, for the guided surface wave with the in-plane momentum $\mathbf{q} \equiv (q_x, q_y)$,

$$\mathbf{E}(\mathbf{r}, t) = \mathbf{E}_{\mathbf{q}}(z) \cdot \exp(iq_x x + iq_y y - i\omega t), \tag{45}$$

$$\mathbf{B}(\mathbf{r}, t) = \mathbf{B}_{\mathbf{q}}(z) \cdot \exp(iq_x x + iq_y y - i\omega t), \tag{46}$$

we obtain

$$\mathbf{E}_{\mathbf{q}}(z) = \begin{cases} (a_s \mathbf{e}_s + a_p \mathbf{e}_p)e^{\kappa_0 z}, & z < 0 \\ a_+ \mathbf{e}_+ e^{-\kappa_+ z} + a_- \mathbf{e}_- e^{-\kappa_- z}, & z > 0 \end{cases}, \tag{47}$$

$$\mathbf{B_q}(z) = \begin{cases} (a_s\mathbf{b}_s + a_p\mathbf{b}_p)e^{\kappa_0 z}, & z < 0 \\ b_+\mathbf{b}_+ e^{-\kappa_+ z} + b_-\mathbf{b}_- e^{-\kappa_- z}, & z > 0 \end{cases}, \tag{48}$$

where the field amplitudes $\mathbf{e}_{s,p}$, $\mathbf{b}_{s,p}$, $\mathbf{e}_\pm$, and $\mathbf{b}_\pm$ are given by

$$\mathbf{e}_s = (q_y, -q_x, 0), \tag{49}$$

$$\mathbf{b}_s = -\frac{c}{\omega}(i\kappa_0 q_x, i\kappa_0 q_y, q_x^2 + q_y^2), \tag{50}$$

$$\mathbf{e}_p = \left[q_x, q_y, -\frac{i}{\kappa_0}(q_x^2 + q_y^2)\right], \tag{51}$$

$$\mathbf{b}_p = \frac{i\omega\epsilon_0}{c\kappa_0}(-q_y, q_x, 0), \tag{52}$$

and

$$\mathbf{e}_\pm = \{i\kappa_\pm q_x[q_y^2 - \Delta_y(\kappa_\pm)], i\kappa_\pm q_y[q_x^2 - \Delta_x(\kappa_\pm)],$$
$$\Delta_x(\kappa_\pm) \cdot \Delta_y(\kappa_\pm) - q_x^2 q_y^2\}, \tag{53}$$

$$\mathbf{b}_\pm = \frac{\omega}{c}\{q_y[\epsilon_y\Delta_x(\kappa_\pm) - \epsilon_x q_x^2], -q_x[\epsilon_x\Delta_y(\kappa_\pm)$$
$$- \epsilon_y q_y^2], iq_x q_y\kappa_\pm(\epsilon_y - \epsilon_x)\}. \tag{54}$$

With nonmagnetic ($\mu = 1$) dielectric materials at both sides of the interface, at $z = 0$, we have the continuity of all three components of the magnetic field $\mathbf{B_q}$, and the continuity of E_x, E_y, and $D_z \equiv \epsilon_z E_z$. However, as follows from Eq. (24), the continuity of both tangential components of the electric field immediately implies the continuity of B_z. Furthermore, since

$$\epsilon_z E_z \propto (\text{curl}B)_z \propto q_x B_y - q_y B_x, \tag{55}$$

the continuity of $D_z = \epsilon_z E_z$ is a direct consequence of the continuity of the tangential magnetic field. Therefore, out of six boundary conditions here only four are actually independent, consistent with the four independent amplitudes a_s, a_p, a_+, and a_-.

Imposing the continuity of E_x, E_y, $\epsilon_z E_z$, and $\partial_z B_z \propto (q_x B_y + q_y B_x)$, we obtain:

$$\mathcal{N}\begin{pmatrix} a_s \\ a_p \\ a_+ \\ a_- \end{pmatrix} = 0, \tag{56}$$

where the matrix $\mathcal{N}$ is defined as

$$\mathcal{N} = \begin{bmatrix} \frac{iq_y}{q_x} & i & \kappa_+(q_y^2 - \Delta_y^+) & \kappa_-(q_y^2 - \Delta_y^-) \\ -\frac{iq_x}{q_y} & i & \kappa_+(q_x^2 - \Delta_x^+) & \kappa_-(q_x^2 - \Delta_x^-) \\ 0 & \frac{iq^2\epsilon_0}{\kappa_0\epsilon_z} & \Delta_x^+\Delta_y^+ - q_x^2 q_y^2 & \Delta_x^-\Delta_y^- - q_x^2 q_y^2 \\ \frac{iq^2\kappa_0}{q_x q_y} & 0 & (\epsilon_y - \epsilon_x)\frac{\omega^2\kappa_+^2}{c^2} & (\epsilon_y - \epsilon_x)\frac{\omega^2\kappa_-^2}{c^2} \end{bmatrix}, \tag{57}$$

with

$$\Delta_{x,y}^\pm \equiv \Delta_{x,y}(\kappa_\pm). \tag{58}$$

Introducing the new variable $\zeta_\pm$ corresponding to the z components of the amplitudes of the electric field in the anisotropic material $(\mathbf{e}_+)_z$ and $(\mathbf{e}_-)_z$:

$$\zeta_\pm = (\Delta_x^\pm\Delta_y^\pm - q_x^2 q_y^2) \cdot a_\pm. \tag{59}$$

From Eqs. (56) and (57), we obtain

$$\begin{pmatrix} \alpha_+ & \alpha_- \\ \beta_+ & \beta_- \end{pmatrix} \cdot \begin{pmatrix} \zeta_+ \\ \zeta_- \end{pmatrix} = 0, \tag{60}$$

where

$$\alpha_\pm = \frac{\epsilon_z}{\epsilon_0} + \frac{\kappa_\pm}{\kappa_0}\frac{(\frac{\omega}{c})^2(\epsilon_x q_y^2 + \epsilon_y q_x^2) - q^2(q^2 - \kappa_\pm^2)}{\Delta_x^\pm\Delta_y^\pm - q_x^2 q_y^2}, \tag{61}$$

$$\beta_\pm = \kappa_\pm \cdot \frac{\kappa_0 + \kappa_\pm}{\Delta_x^\pm\Delta_y^\pm - q_x^2 q_y^2}. \tag{62}$$

The dispersion of the surface wave is then given by

$$\det\begin{pmatrix} \alpha_+ & \alpha_- \\ \beta_+ & \beta_- \end{pmatrix} = 0, \tag{63}$$

which yields

$$\kappa_0(\kappa_+ + \kappa_-) \cdot \left\{\frac{\epsilon_x\epsilon_y}{\epsilon_0}\left[\left(\frac{\omega}{c}\right)^2 - \frac{q_x^2}{\epsilon_y} - \frac{q_y^2}{\epsilon_x}\right] - \kappa_+\kappa_-\right\}$$
$$+ \kappa_+\kappa_-\left[(\epsilon_x + \epsilon_y)\left(\frac{\omega}{c}\right)^2 - \frac{\epsilon_0 + \epsilon_x}{\epsilon_0}q_x^2 - \frac{\epsilon_0 + \epsilon_y}{\epsilon_0}q_y^2\right]$$
$$+ \left\{\frac{\epsilon_x\epsilon_y}{\epsilon_0}\kappa_0^2\left[\left(\frac{\omega}{c}\right)^2 - \frac{q_x^2}{\epsilon_y} - \frac{q_y^2}{\epsilon_x}\right] - \kappa_+^2\kappa_-^2\right\} = 0. \tag{64}$$

Equation (47) uniquely defines the dispersion relation of the Dyakonov surface wave $\omega(\mathbf{q})$ and immediately leads to Eq. (15) in the main body of this paper.

References

1. V. G. Veselago, "The electrodynamics of substances with simultaneously negative values of ϵ and μ," *Sov. Phys. Usp.* **10**(4), 509–514 (1968).
2. J. B. Pendry, "Negative refraction makes a perfect lens," *Phys. Rev. Lett.* **85**, 3966–3969 (2000).
3. R. A. Shelby, D. R. Smith, and S. Schultz, "Experimental verification of a negative index of refraction," *Science* **292**(5514), 77–79 (2001).
4. D. Schurig et al., "Metamaterial electromagnetic cloak at microwave frequencies," *Science* **314**(5801), 977–980 (2006).
5. A. Grbic and G. V. Eleftheriades, "Negative refraction, growing evanescent waves and sub-diffraction imaging in loaded-

transmission-line metamaterials," *IEEE Trans. Microwave Theory Tech.* **51**(12), 2297–2305 (2003).

6. Z. Liu et al., "Rapid growth of evanescent wave by a silver super-lens," *Appl. Phys. Lett.* **83**(25), 5184 (2003).

7. R. Merlin, "Metamaterials and the Landau—Lifshitz permeability argument: large permittivity begets high-frequency magnetism," *Proc. Nat. Acad. Sci. U. S. A.* **106**(6), 1693–1698 (2008).

8. C. Luo, S. G. Johnson, and J. D. Joannopoulos, "All-angle negative refraction in a three-dimensionally periodic photonic crystal," *App. Phys. Lett.* **81**(13), 2352 (2002).

9. M. S. Wheeler, J. S. Aitchison, and M. Mojahedi, "Coated non-magnetic spheres with a negative index of refraction at infrared frequencies," *Phys. Rev. B* **73**, 045105 (2006).

10. W. Can and V. Shalaev, *Optical Metamaterials: Fundamentals and Applications*, Springer, New York (2010).

11. The situation is similar in polaritonic materials in mid-IR wave-length range, where the negative permittivity originated from resonant coupling to optical phonons, with the concomitant "resonant" loss.

12. V. A. Podolskiy and E. E. Narimanov, "Near-sighted superlens," *Opt. Lett.* **30**(1), 75–77 (2005).

13. G. V. Naik, V. M. Shalaev, and A. Boltasseva, "Alternative plasmonic materials: beyond gold and silver," *Adv. Mater.* **25**(24), 3264–3294 (2013).

14. S. Xiao et al., "Loss-free and active optical negative-index metamaterials," *Nature* **466**, 735–738 (2010).

15. J. B. Khurgin and G. Sun, "In search of the elusive lossless metal," *Appl. Phys. Lett.* **96**, 181102 (2010).

16. M. Kuś, F. Haake, and D. Delande, "Prebifurcation periodic ghost orbits in semiclassical quantization," *Phys. Rev. Lett.* **71**, 2167–2171 (1993).

17. H. C. Chen, *Theory of Electromagnetic Waves: A Coordinate-Free Approach*, McGraw-Hill, New York (1983).

18. A. Salandrino and D. N. Christodoulides, "Negative index Clarricoats-Waldron waveguides for terahertz and far infrared applications," *Opt. Express* **18**(4), 3626–3631 (2010).

19. L. V. Alekseyev and E. Narimanov, "Slow light and 3-D imaging with non-magnetic negative index systems," *Opt. Express* **14**(23), 11184–11193 (2006).

20. J. Nemirovsky, M. C. Rechtsman, and M. Segev, "Negative radiation pressure and negative effective refractive index via dielectric birefringence," *Opt. Express* **20**(8), 8907–8914 (2012).

21. L. E. Reichl, *The Transition to Chaos in Conservative Classical Systems: Quantum Manifestations*, Springer-Verlag, New York (1992)

22. F. Haake, *Quantum Signatures of Chaos*, Springer, New York (2010).

23. R. Scharf and B. Sundaram, "Traces of ghost orbits in the quantum standard map," *Phys. Rev. E* **49**, R4767 (1994).

24. T. Bartschdag, J. Maindag, and G. Wunnerddag, "Significance of ghost orbit bifurcations in semiclassical spectra," *J. Phys. A: Math. Gen.* **32**(16), 3013–3027 (1999).

25. B. Grémaud and D. Delande, "Ghost orbits in the diamagnetic hydrogen spectrum using harmonic inversion," *Phys. Rev. A* **61**, 032504 (2000).

26. R. Wangberg et al., "Non-magnetic nano-composites for optical and infrared negative refraction index media," *J. Opt. Soc. Am. B* **23**(3), 498–505 (2006).

27. S. Ramo, J. R. Whinnery, and T. Van Duzer, *Fields and Waves in Communication Electronics*, 3rd ed., John Wiley & Sons, Inc., Hoboken, New Jersey (1994).

28. S. Hirotsu, T. Yanagi, and S. Sawada, "Refractive indices of $NaNO_2$ and anisotropic polarizability of NO_2^-," *J. Phys. Soc. Jpn.* **25**(3), 799–807 (1968).

29. W. R. Hamilton, "Third supplement to an essay on the theory of systems of rays," *Trans. R. Irish Acad.* **17**, 1–144 (1837).

30. H. Lloyd, "On the phenomena presented by light in its passage along the axes of biaxial crystals," *Trans. R. Irish Acad.* **17**, 145–157 (1833).

31. R. Potter, "An examination of the phenomena of conical refraction in biaxial crystals," *Lond., Edinburgh Dublin Philos. Mag. J. Sci.* **18**(3), 343–353 (1841).

32. M. V. Berry, M. R. Jeffrey, and J. G. Lunney, "Conical diffraction: observations and theory," *Proc. R. Soc. A* **462**, 1629–1642 (2006).

33. M. V. Berry and M. R. Jeffrey, "Conical diffraction: Hamiltons diabolical point at the heart of crystal optics," *Prog. Opt.* **50**, 13–50 (2007).

34. C. V. Raman, "Conical refraction in biaxial crystals," *Nature* **107**, 747 (1921).

35. D. P. O'Dwyer et al., "Optical trapping using cascade conical refraction of light," *Opt. Express* **20**(19), 21119–21125 (2012).

36. Z. Huang and E. E. Narimanov, "Optical phase retrieval using conical refraction in structured media," *Opt. Lett.* **41**(23), 5567–5570 (2016).

37. J. D. Joannopoulos et al., *Photonic Crystals: Molding the Flow of Light*, Princeton University Press, Princeton (2008).

38. F. D. M. Haldane, "Electromagnetic surface modes at interfaces with negative refractive index make a 'not-quite-perfect' lens," https://arxiv.org/abs/cond-mat/0206420 (2002).

39. M. I. Dyakonov, "New type of electromagnetic wave propagating at an interface," *Sov. Phys. JETP* **67**(4), 714 (1988).

40. D. B. Walker, E. N. Glytsis, and T. K. Gaylord, "Surface mode at isotropic-uniaxial and isotropic-biaxial interfaces," *J. Opt. Soc. Am.* **15**, 248–260 (1998).

41. O. Takayama et al., "Dyakonov surface waves: a review," *Electromagnetics* **28**(3), 126–145 (2008).

42. L. D. Landau and E. M. Lifshitz, *Electrodynamics of Continuous Media*, 2nd ed., Elsevier Butterworth-Heinemann, Oxford (1984).

43. R. Merlin, "Analytical solution of the almost-perfect-lens problem," *Appl. Phys. Lett.* **84**(8), 1290 (2004).

Evgenii Narimanov is a professor of electrical and computer engineering at Purdue University. He is a fellow of OSA and IEEE.